



COMMUNICATION

[View Article Online](#)
[View Journal](#) | [View Issue](#)Cite this: *Mater. Horiz.*, 2024,
11, 454Received 22nd August 2023,
Accepted 6th November 2023

DOI: 10.1039/d3mh01336g

rsc.li/materials-horizonsDeciphering the anisotropic energy harvesting
responses of an above room temperature
molecular ferroelectric copper(II) complex single
crystal†Rajashi Haldar,^{‡a} Ajay Kumar,^{‡b} Dipankar Mandal ^{*b} and
Maheswaran Shanmugam ^{*a}

The mechanical/piezoelectric and/or thermal/pyroelectric energy harvesting efficiency is observed to be extremely good in multi-component ferroelectric inorganic oxides in their single-crystal form rather than in their polycrystalline counterparts (pellets and thick/thin films). However, growing such multi-component single crystals is a challenging and cost-intensive process besides the difficulty in tuning their long-range ferroic ordering and the involvement of toxic heavy elements. Instead, discrete inorganic metal complexes can be potential alternatives for which one can overcome these caveats by an appropriate design strategy. Herein, we report a biocompatible and an above room temperature ($T_c > 380$ K) molecular ferroelectric $[\text{Cu}_2(\text{L-phe})_2(\text{bpy})_2(\text{H}_2\text{O})](\text{ClO}_4)_2 \cdot 2\text{H}_2\text{O}$ single crystal (**1**) with profound anisotropic piezo- and pyroelectric responses along different unit cell axes. Energy harvesting data at room temperature reveal that the highest possibility of scavenging mechanical energy ($\sim 30 \mu\text{W m}^{-2}$) is preferentially along the *b*-axis. This is attributed to the large spontaneous polarization ($P_s = 2.5 \mu\text{C cm}^{-2}$) and piezoelectric coefficient ($d_{33} = 23.5 \text{ pm V}^{-1}$) observed along the *b*-axis, compared to those along the other two axes. The highest output voltage (7.4 V cm^{-2}) and pyroelectric coefficient ($29 \mu\text{C m}^{-2} \text{ K}^{-1}$) obtained for the single-crystal device are impressively higher than those of most of the reported materials. Such a molecular anisotropic single-crystal piezo-/pyroelectric nanogenerator (SC-PENG) with excellent mechanical and thermal energy harvesting competence is reported for the first time.

Introduction

Scavenging energies that are abundant, but are mostly lost or wasted (such as vibrations, pressure or heat) and converting

New concepts

Achieving room temperature phase transitions and polar point groups in discrete inorganic complex-based ferroelectric materials presents an intricate challenge. This obstacle has been surmounted through a judicious molecular engineering strategy. This strategy not only led us to isolate $[\text{Cu}_2(\text{L-Phe})_2(\text{bpy})_2(\text{H}_2\text{O})](\text{ClO}_4)_2 \cdot 2\text{H}_2\text{O}$ (**1**) but also revealed the phase transitions occurring at significantly elevated temperatures ($T_c > 380$ K). The domain of harvesting different forms of sustainable energy (such as mechanical, thermal, and acoustic) has been dominated by conventional bulk oxide based nanogenerators. However, the development of these materials is constrained by issues such as heavy metal toxicity, brittleness, and poor chemical control, stymieing their progress. In light of these challenges, the integration of devices using **1** for sustainable energy harvesting is a conspicuously rare pursuit, especially in the context of employing single crystals directly for energy conversion. Remarkably, the single crystal-PENG exhibits unparalleled anisotropic responses, alongside an impressive output voltage (7.4 V cm^{-2}) and an exceptional piezo/pyroelectric coefficient, outperforming many traditional oxides, semiconductors, and polymers. The revealed design principles and output efficiencies of **1** are set to usher in a transformative era of sustainable energy, prompting a paradigm shift. The findings outlined in this manuscript stand to unlock revolutionary prospects for self-powered devices, offering tangible and scalable solutions for real-world sustainability challenges.

them into more useful electrical energy using various energy-harvesting nanogenerators is one of the cutting-edge areas of research at present.^{1,2} Such self-powered piezo-/tribo-/pyroelectric nanogenerators can provide clean, sustainable and smart alternatives to conventional batteries due to their low-maintenance and long lifespans and can operate even in remote locations. Due to their superior ferro- and piezoelectric properties, inorganic bulk oxides (perovskites and

^a Department of Chemistry, Indian Institute of Technology Bombay, Powai, Mumbai-400076, India. E-mail: eswar@chem.iitb.ac.in^b Quantum Materials and Devices Unit, Institute of Nano Science and Technology, Knowledge City, Sector 81, Mohali 140306, India. E-mail: dmandal@inst.ac.in† Electronic supplementary information (ESI) available: Detailed synthetic procedures, X-ray structural data and their descriptions along with crystallographic and structural parameters, TGA-DTA thermograms, DSC, variable temperature powder XRD data, dielectric data, vector PFM, and *I*-*V* data. CCDC 2284226 and 2284227. For ESI and crystallographic data in CIF or other electronic format see DOI: <https://doi.org/10.1039/d3mh01336g>

‡ Authors contributed equally to this work.

ceramics) have ruled the fields of energy harvesters, sensors and actuators for decades, but their bio-incompatibility, heavy metal toxicity, poor tunability of long-range properties, brittleness, and costly manufacturing processes have been the biggest barriers to realizing their practical applications. Low output responses, complicated device fabrication and shorter life-spans are the major obstacles for other PENG devices based on flexible polymers and bioorganic materials including peptides.^{3–6} Also, the energy harvesting performance is generally tested either on polycrystalline pellets or composite films but their efficiency is expected to be low compared to the devices made up of pure multi-component single crystals with enhanced electrical, mechanical, thermal, and optical responses.^{7,8} For example, a multi-component single crystal unimorph of PMN-PT or PIN-PMN-PT exhibits an ultrahigh piezoelectric performance as compared to the single crystals of classical PZT and its polycrystalline samples. However, growing such multi-component single crystals in larger dimensions is an extremely challenging process, and hence they have been reported only in a handful of studies.⁹

By a low cost, precise design strategy and simple synthetic process, we have unveiled a discrete molecular ferroelectric $[\text{Cu}_2(\text{L-phe})_2(\text{bpy})_2(\text{H}_2\text{O})](\text{ClO}_4)_2 \cdot 2\text{H}_2\text{O}$ (**1**; where L-Phe = L-phenylalanine, bpy = 2,2'-bipyridine) that not only shows superior piezo- and ferroelectric properties ($P_s = 2.5 \mu\text{C cm}^{-2}$ and $d_{33} = 23.5 \text{ pm V}^{-1}$), but also has a Curie temperature (T_c) well above the room temperature ($> 380 \text{ K}$), which is quite rare for molecular complexes.¹⁰ The energy harvesting responses recorded on a single crystal of **1** show distinct anisotropic responses along different unit cell axes and yield an open-circuit voltage value of 7.4 V cm^{-2} along the *b*-axis with a power density of $30 \mu\text{W m}^{-2}$. This electrical output is one of the largest outputs among the discrete molecular PENG devices reported in the literature and is comparable to those of certain conventional bulk oxide devices.^{3,11,12} We also report the pyroelectric

energy harvesting of the single crystal of **1** (along the *b*-axis) with a pyroelectric coefficient of $29 \mu\text{C m}^{-2} \text{ K}$. To the best of our knowledge, this is the first report on single-crystal anisotropic mechanical and thermal energy harvesting based on a discrete molecular complex.

Results and discussion

The dark blue, block-shaped crystals of **1** were obtained at room temperature upon slow evaporation of the reaction mixture of $\text{CuSO}_4 \cdot 5\text{H}_2\text{O}$, L-phe and bpy in the water-ethanol solvent (Scheme S1, ESI†).¹³ Single crystal data collection was performed at low temperature (150 K) and at room temperature (300 K) shows that there are no significant changes in the unit cell parameters at both of these temperatures (Table S1, ESI†). Therefore, the structural details of **1** collected at room temperature are provided below. The structure solution reveals the molecular formula of **1** as $[\text{Cu}_2(\text{L-phe})_2(\text{bpy})_2(\text{H}_2\text{O})](\text{ClO}_4)_2 \cdot 2\text{H}_2\text{O}$ (**1**), which crystallizes in the monoclinic, non-centrosymmetric $P2_1$ space group and adopts a dimeric structure (Fig. 1a). Although both copper centres exhibit a distorted square pyramidal geometry, their coordination environments are slightly different from each other. Four of their five coordination sites are completed by chelating bpy and L-phe ligands.



Maheswaran Shanmugam

Ever since our inaugural publication in Materials Horizons back in early 2019, we have cultivated a lasting alliance with this exceptional journal. Our way of showing appreciation to the Materials Horizons' community has been through the consistent sharing of our noteworthy scientific endeavors. Presently, we are excited to reveal our latest research, delving into the anisotropic mechanical and thermal energy harvesting within a single crystal device. We take great

pleasure in presenting these remarkable findings within the distinguished platform of 'Materials Horizons', and eagerly look forward to continuing this journey together, with the promise of contributing more captivating work in the future. Congratulations on the journal's 10th anniversary and best wishes to Materials Horizons!

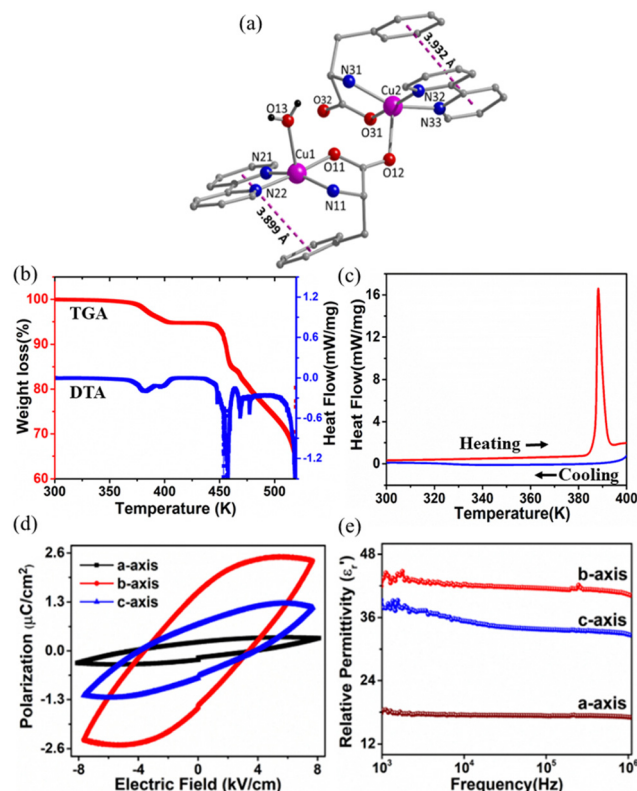


Fig. 1 (a) Ball and stick representation of crystal structure of **1**. The Hydrogen atoms are omitted for clarity. (b) TGA-DTA thermograms of **1**, (c) DSC curves of **1**, (d) and (e) direction dependent polarization vs. electric field (*P*–*E*) hysteresis loop and relative permittivity (ϵ_r) vs. frequency (10^3 – 10^6 Hz) measured along *a*, *b* and *c*-axes respectively on a single crystal of **1**.

The fifth coordination site of one Cu(II) ion is filled by a terminal water (Cu1–O13 = 2.273(4) Å) molecule, and for the other site, it is completed by the bridging carboxylate atom (Cu2–O12 = 2.242(3) Å) derived from L-phe, which are the typical Jahn–Teller orientations of these two Cu(II) centers. The average Cu–N bond distances were observed to be Cu–N_{bpy} = 1.991(6) Å and Cu–N_{amine} = 2.007(5) Å, while the average Cu–O bond length was observed to be 1.933(5) Å (Fig. S1 and Table S2, ESI†). Two ClO₄ anions residing in the crystal lattice neutralize the overall +2 charge on the coordination sphere. The packing diagram of **1** (Fig. S2, ESI†) reveals that the perchlorate anions and the solvate water molecules occupy the crystal lattice in between the layers of these dinuclear molecular arrangements and are involved in the intermolecular hydrogen bonding, e.g. N11–H11B...O13A_1 with $d = 2.995(5)$ Å and symmetry code \$1 = -x + 2, y - 0.5, -z + 2\$; O1S–H1SA...O32_2 with $d = 2.734(5)$ Å and symmetry code \$2 = x + 1, y, z\$; and O1S–H1SB...O21A_3 with $d = 2.974(7)$ Å and symmetry code \$3 = -x + 1, y + 0.5, -z + 1\$ (Table S3, ESI†). The 2D-fingerprint data obtained from the Hirshfeld analysis confirm that nearly 40% of the intermolecular interactions were mediated by these anions and water molecules (Fig. S3, ESI†).

No apparent weight loss of the sample up to 370 K is observed, signifies the thermal stability of **1** during thermogravimetric analysis (TGA; Fig. 1b). Above this temperature and up to 406 K, there is a continuous weight loss (4.45%), which is attributed to the loss of solvate water and the water molecule coordinated to the Cu1 centre (Fig. 1a). The loss of the solvate water molecule causes no structural change (≤ 380 K), while with the loss of coordinated water molecule (above 380 K), the structure of **1** changes drastically, which is firmly supported by the variable temperature powder X-ray diffraction (VT-PXRD) measurement (Fig. S4, ESI†). Below 380 K, the VT-PXRD profile is in excellent agreement with that of room temperature data, implying that not only the bulk phase purity but also the polar space group of **1** was maintained below 380 K. Consistent with TGA and VT-PXRD measurements, there is no thermal anomaly observed in differential scanning calorimetry (DSC) measurements until 380 K, while melting of the sample begins above 380 K and shows a sharp maximum at 390 K in the heating cycle (Fig. 1c). The release of the coordinated water molecule from the metal centre coupled with the melting of the crystal does not allow the recovery of the initial ferroelectric phase of **1** upon cooling (see Fig. 1c).

The large block-shaped crystals ($2.6 \times 4.9 \times 5.2$ mm³) of **1** allowed us to perform ferroelectric hysteresis loop (polarization (P) vs. electric field (E)) measurements on a single crystal in all three directions a , b and c , characterized by the face-indexing of the crystal (Fig. S5, ESI†) at room temperature. Such studies are rare, due to the complications in synthesizing bigger single crystals of bulk oxides, inorganic–organic hybrid perovskites and other molecular complexes. The maximum spontaneous polarization (P_s) values obtained are 0.3, 2.5 and 1.2 $\mu\text{C cm}^{-2}$ in a -, b - and c -directions respectively (Fig. 1d), which are relatively high compared to many of the reported molecular ferroelectrics.^{14–16} In the crystal lattice of **1**, along the b -axis the molecules (cations and anions) are related by the 2₁ screw axis

symmetry, while such a crystallographically imposed symmetry is not found along the a - and c -axes. Hence, along the b -axis, the dipole alignment and various supramolecular interactions (like hydrogen bonding, π – π interactions, anion– π interactions, CH– π interactions) are stronger compared to those along the other two axes (resulting in low P_s values along the a and c -axes). This facile alignment of dipoles along the b -axis is not only responsible for the anisotropic ferroelectric responses (*vide supra*),^{17–19} but also responsible for the dielectric/pyroelectric/piezoelectric responses (*vide infra*). A similar trend in anisotropy is reflected in the frequency-dependent relative dielectric permittivity (ϵ_r') measurement, where the plot of ϵ_r' vs. ν reveals that ϵ_r' is again larger along the b -axis ($\epsilon_r'(b) = 42$) compared to those along the other two orthogonal axes ($\epsilon_r'(a) = 17$ and $\epsilon_r'(c) = 36$) at 1 kHz (Fig. 1e).

In the temperature dependent ϵ_r' measurement, we did not observe any dielectric anomaly up to 375 K. The ϵ_r' value drastically increases upon increasing the temperature further, due to the onset of melting of the crystal (Fig. S6a, ESI†). Therefore, the polar point group signature of **1** is well maintained up to 370 K and the ferroelectric to paraelectric transition temperature (Curie temperature, T_c) lies above its melting point.^{19,20} Hence, in order to maintain the ferroelectric behaviour of the system and avoid melting, the crystals should not be heated beyond 370 K. Generally, the T_c of such discrete molecules is mostly observed to be well below room temperature, which has long been a bottleneck restricting their use in energy-harvesting applications. However, thanks to appropriate molecular design, we were able to achieve an above-room temperature ferroelectric complex by introducing long range supramolecular interactions. The dielectric loss ($\tan \delta$) for **1** (Fig. S6b, ESI†) is observed to be low (< 0.5) below 375 K, but it is relatively high as compared to that of the traditional ferroelectric piezoceramics ($\tan \delta \sim 0.2$). In certain piezoceramics like ZnO, such higher values of dielectric loss are observed due to their semiconducting nature, as witnessed in many literature reports.^{21,22} To support this statement, we have performed $\tan \delta$ measurements on the semiconducting wurtzite phase (JCPDS no. 36-1451) comprising zinc oxide (ZnO). The piezoelectric phase ZnO exhibits a $\tan \delta$ value of ~ 2 at 10 kHz, which is quite higher than that of usual piezoceramics due to the semiconducting nature of ZnO (Fig. S7, ESI†). In the case of **1**, the value of $\tan \delta$ (~ 0.5) is slightly higher than that of the conventional piezoceramics such as BTO or PZT, which is attributed to the semiconducting behaviour of the system due to the presence of Cu²⁺ metal ions (d^9 system) in **1**. The semiconducting nature of **1** is evident from the I – V measurement (Fig. S8, ESI†). This effect is higher along the a - and c -axes, leading to lossy P – E loops along these directions as compared to that along the b -axis.

To further firmly confirm the ferroelectric phenomenon associated with **1**, the direction-dependent local ferroelectric response on the single crystals of **1** was verified by piezo-response force microscopy (PFM), performed at room temperature by employing the AC bias along three directions. The phase

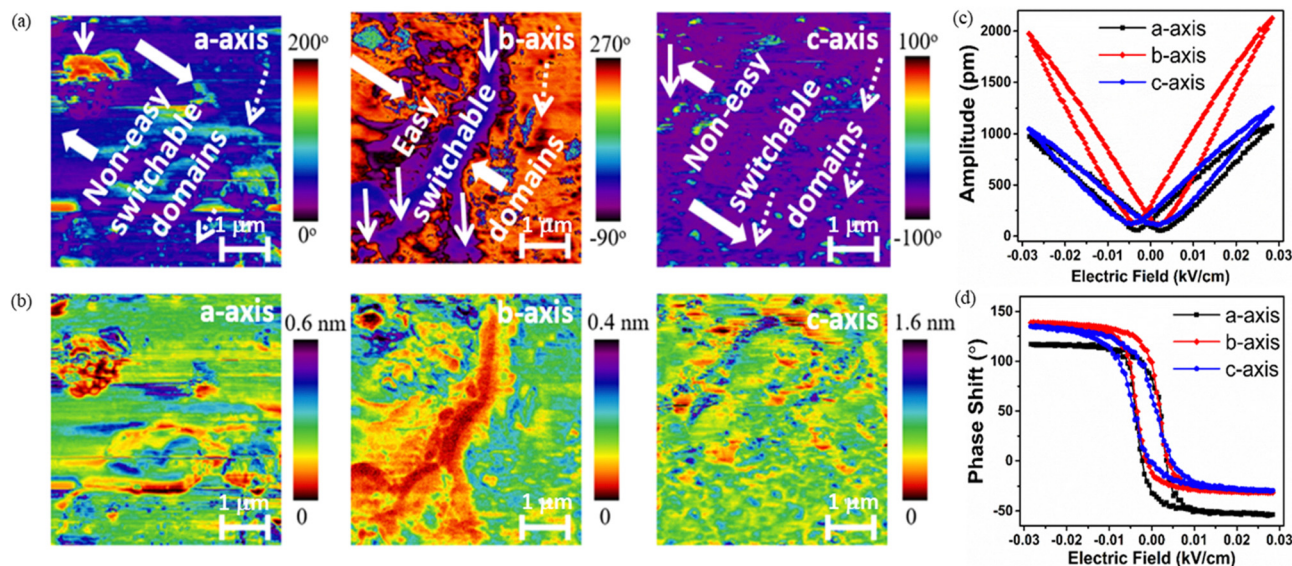


Fig. 2 (a) Vertical PFM phase images recorded on a single crystal of **1** oriented along *a*-, *b*- and *c*-axis and (b) corresponding amplitude images showing the different domains, (c) amplitude vs. electric field butterfly loop, (d) phase shift vs. electric field hysteresis loop along the three directions (applied voltage is normalized with respect to electric field).

(Fig. 2a) and amplitude images (Fig. 2b) along the *b*-axis indicate that in this direction the population of more energetically favourable (switchable) 180° ferroelectric domains (indicated by solid arrows) is higher than that of the unfavourable switchable domains (indicated by dotted arrows). In contrast, the phase and amplitude images along the *a*- and *c*-axes demonstrate a higher population of twisted (rotated) ferroelectric domains. These different population distributions of domains along the three axes account for the anisotropic piezoelectric responses.²³ Consequently, similar types of domain patterns are also observed in the lateral PFM image (Fig. S9, ESI†). From the butterfly loops (amplitude vs. electric field curves; Fig. 2c), obtained in the switching spectroscopy (SS-PFM) study, the calculated piezoelectric coefficients (d_{33}) are 16.8 ± 0.3 , 23.5 ± 0.6 , and 17.7 ± 0.4 pm V⁻¹ along the *a*-, *b*- and *c*-axes, respectively, which are higher than those of some of the inorganic oxides like ZnO, CdS, GaN, and LiNbO₃, organic-inorganic hybrid systems, most of the biomaterials, and discrete molecular complexes.²⁴ d_{33} values were calculated using the equation, $d_{33} = \Delta z/V$, where Δz is the deflection of the cantilever caused by the deformation of ferroelectric samples under an applied electric field and V is the applied voltage due to the converse piezoelectric effect and can be calculated from the slope of the linear part of the amplitude vs. voltage curve (butterfly loop).²⁵ The 180° phase shift in the phase loop (the phase vs. electric field plot), obtained in all three directions, confirms the piezo- and ferroelectric nature of **1** (Fig. 2d).

Noteworthy, the estimated d_{33} (11.9 ± 0.2 pm V⁻¹) and P_s (0.2 μC cm⁻²) values for the polycrystalline sample (pressed pellets) of **1** is quite low, and the P - E loop is much lossier than that of the single crystal (Fig. S10 and S11, ESI†). The polycrystalline pellets are prepared by compressing and sintering the powdered material, which leads to defects, porosity, and

local mechanical inhomogeneity due to residual stress. In contrast, single crystals provide more efficient, homogeneous, and accurate electrical, mechanical, and thermal responses. This inspired us to test the direction-dependent piezoelectric energy harvesting capability directly on a single crystal of **1**.

Fig. 3a shows the schematic of the electrode connection along the *a*-, *b*-, and *c*-axes of the crystal. The piezoelectric responses from the different axes were collected under the cyclic load of 6 N. It is observed that the unpoled *a*-, *b*- and *c*-axes yield voltage responses of 1.3 V cm⁻², 1.9 V cm⁻², and 0.6 V cm⁻² respectively, which increased in a poled crystal to 2.6 V cm⁻² along the *a*-axis, 7.4 V cm⁻² along the *b*-axis and 2.7 V cm⁻² along the *c*-axis (Fig. 3b-d). This indicates that the dipole alignment in all three directions is feasible, but the higher saturation polarization and degree of dipole population along the *b*-axis lead to a higher voltage in this direction with a response time of ~10 ms. Fig. 3e shows the current vs. time response for the unpoled and poled *b*-axes of **1** with a maximum current of 4.5 μA cm⁻² in the poled crystal. From the power density curve (Fig. 3f) we find that it is possible to harvest 30 μW m⁻² power from the bare crystal.

Furthermore, the spontaneous polarization coupled pyroelectric response measurement was performed at room temperature (300 K) along the *b*-axis. Fig. 4a(i-iii) indicates that the increase in temperature difference from 0.9 °C to 6.7 °C leads to an increase in pyroelectric current (i_p) of up to 300 pA for a 1.8 °C s⁻¹ rate of change of temperature (Fig. S12, ESI†). The enhanced i_p is attributed to a faster temporal change in temperature (ΔT). The pyroelectric coefficient of the crystal was calculated using the following equation,

$$i_p = A p_r \frac{dT}{dt}$$

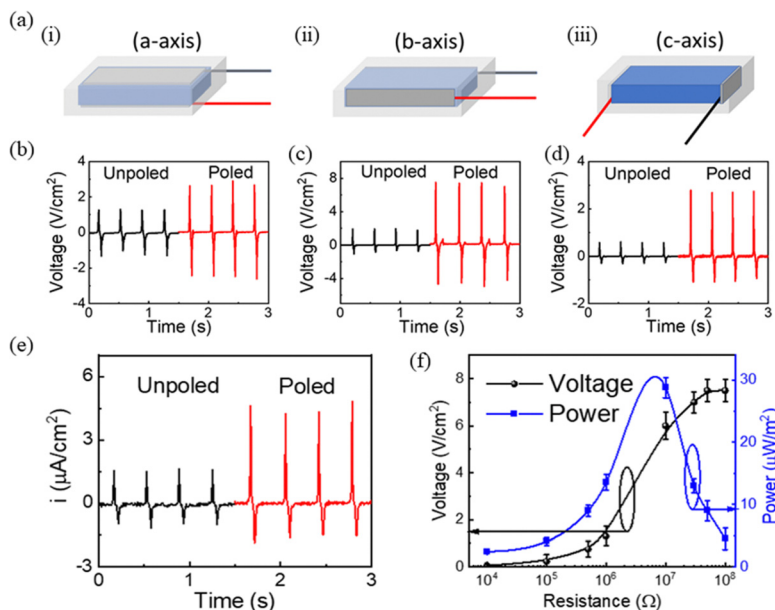


Fig. 3 (a) Schematic of electrode connection in (i) *a*-, (ii) *b*- and (iii) *c*-axis on a single crystal of **1** with corresponding voltage vs. time response in poled and unpoled device along (b) *a*-, (c) *b*- and (d) *c*-axis under cyclic load of 6 N. (e) Current vs. time response of poled and unpoled device along *b*-axis. (f) Normalized voltage vs. resistance and power density curve along the *b*-axis.

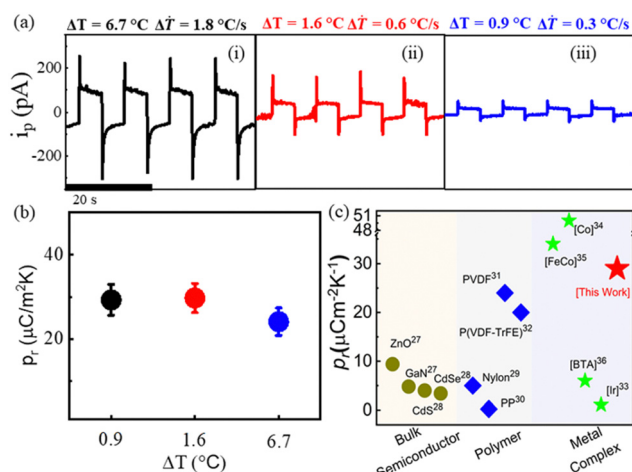


Fig. 4 (a) Pyroelectric response along *b*-axis under temporal change in temperature of (i) 6.7 °C ($\Delta T = 1.8 \text{ }^{\circ}\text{C s}^{-1}$), (ii) 1.6 °C ($\Delta T = 0.6 \text{ }^{\circ}\text{C s}^{-1}$) and (iii) 0.9 °C ($\Delta T = 0.3 \text{ }^{\circ}\text{C s}^{-1}$), (b) pyroelectric coefficient as a function of temperature change and (c) comparison of pyroelectric coefficient in different materials (ref. 26–36).

where T is the temperature, t is the time, A is the area of the electrode and p_r is the pyroelectric coefficient.

The observed pyroelectric coefficient of $29 \text{ } \mu\text{C m}^{-2} \text{ K}^{-1}$ and response time of 0.12 s are constant under different temperature changes (Fig. 4b) and the values are much higher than those of the well-known pyroelectric bulk semiconductors (*i.e.*, ZnO, CdS, CdSe, and GaN), ferroelectric polymers (*i.e.*, PVDF, P(VDF-TrFE), and odd nylons) and most of the reported metal complexes at room temperature (Fig. 4c).^{26–33} Hence, our work contributes to the ongoing investigation of the

pyroelectric energy harvesting efficiencies of discrete molecular systems.^{34–36}

Conclusions

To conclude, the discrete molecular, above room temperature ferroelectric complex **1** shows significantly anisotropic ferro-/piezo-/di-electric responses along different axes in its single crystal form and the values are substantially higher compared to its polycrystalline form. The poled SC-PENG device made of **1** shows the highest open circuit output voltage of 7.4 V cm^{-2} . We have also exploited the pyroelectric properties of **1** for waste heat energy harvesting with an appreciable pyroelectric coefficient of $29 \text{ } \mu\text{C m}^{-2} \text{ K}^{-1}$. We have established that the efficiency of energy harvesting is significantly higher in a single crystal of **1** compared to that in its polycrystalline form. In contrast to the single crystals of conventional bulk oxides, single crystals of discrete molecular complexes are easier to synthesize and can be envisaged for various other applications such as anisotropic sensors, ultrasound transducers, and acoustic devices so as to avoid multidirectional mechanical and heat flux fluctuation aided artifacts. This opens up a lot of possibilities for molecular complexes in real-world applications.

Author contributions

RH carried out the synthesis of the complex and performed single crystal XRD, PFM, and other analyses related to the material. AK made the devices and investigated the energy harvesting responses (both piezo and pyro). MS and DM envisioned and planned the entire work. All authors have contributed to the writing of the manuscript.

Conflicts of interest

There are no conflicts to declare.

Acknowledgements

MS thanks the funding agencies BRNS (58/14/07/2023-BRNS/37029), SUPRA (SPR/2019/001145), CSIR (01(2933)/18/EMR-II), SERB and IIT Bombay for financial support. DM is grateful to the Science and Engineering Research Board (CRG/2020/004306), the Government of India, for financial support. RH is thankful to Mr Vijay Mistari for his help with the recording of PFM data, IIT Bombay for providing various facilities and Prime Minister's Research Fellowship for financial assistance. AK is thankful to the University Grant Commission for awarding the fellowship.

References

- 1 C. R. Bowen, H. A. Kim, P. M. Weaver and S. Dunn, *Energy Environ. Sci.*, 2014, **7**, 25–44.
- 2 T. Li and P. S. Lee, *Small Struct.*, 2022, **3**, 2100128.
- 3 T. Vijayakanth, D. J. Liptrot, E. Gazit, R. Boomishankar and C. R. Bowen, *Adv. Funct. Mater.*, 2022, **32**, 2109492.
- 4 S. Sukumaran, S. Chatbouri, D. Rouxel, E. Tisserand, F. Thiebaud and T. Ben Zineb, *J. Intell. Mater. Syst. Struct.*, 2021, **32**, 746–780.
- 5 C. Sohn, H. Kim, J. Han, K. T. Lee, A. Šutka and C. K. Jeong, *Nano Energy*, 2022, **103**, 107844.
- 6 Y. Wang, S. Liu, L. Li, H. Li, Y. Yin, S. Rencus-Lazar, S. Guerin, W. Ouyang, D. Thompson, R. Yang, K. Cai, E. Gazit and W. Ji, *J. Am. Chem. Soc.*, 2023, **145**, 15331–15342.
- 7 C. Sun, L. Qin, F. Li and Q. M. Wang, *J. Intell. Mater. Syst. Struct.*, 2009, **20**, 559–568.
- 8 B. Murali, H. K. Kolli, J. Yin, R. Ketavath, O. M. Bakr and O. F. Mohammed, *ACS Mater. Lett.*, 2020, **2**, 184–214.
- 9 M. Ma, S. Xia, X. Gao, K. Song, H. Guo, F. Li, Z. Xu and Z. Li, *Appl. Phys. Lett.*, 2022, **120**, 078609.
- 10 H. Y. Zhang, Y. Y. Tang, P. P. Shi and R. G. Xiong, *Acc. Chem. Res.*, 2019, **52**, 1928–1938.
- 11 T. Vijayakanth, F. Ram, B. Praveenkumar, K. Shanmuganathan and R. Boomishankar, *Angew. Chem., Int. Ed.*, 2020, **59**, 10368–10373.
- 12 R. Halder, A. Kumar, B. Mallick, S. Ganguly, D. Mandal and M. Shanmugam, *Angew. Chem., Int. Ed.*, 2023, **62**, 202216680.
- 13 P. S. Subramanian, E. Suresh, P. Dastidar, S. Waghmode and D. Srinivas, *Inorg. Chem.*, 2001, **40**, 4291–4301.
- 14 J. Valasek, *Phys. Rev.*, 1921, **17**, 471–481.
- 15 P. P. Shi, Y. Y. Tang, P. F. Li, W. Q. Liao, Z. X. Wang, Q. Ye and R. G. Xiong, *Chem. Soc. Rev.*, 2016, **45**, 3811–3827.
- 16 M. Wasim, K. U. Ansari, P. Kumar, B. Mallick and M. Shanmugam, *Inorg. Chem. Front.*, 2022, **9**, 2284–2289.
- 17 J. F. Nye, *Physical Properties of Crystals. Their Representation by Tensors and Matrices*, Clarendon Press, 1957.
- 18 M. Wojtaś, V. Kinzhybalov, I. Bdikin and A. L. Kholkin, *Cryst. Growth Des.*, 2019, **19**, 2583–2593.
- 19 J. Long, M. S. Ivanov, V. A. Khomchenko, E. Mamontova, J. M. Thibaud, J. Rouquette, M. Beaudhuin, D. Granier, R. A. S. Ferreira, L. D. Carlos, B. Donnadieu, M. S. C. Henriques, J. A. Paixão, Y. Guari and J. Larionova, *Science*, 2020, **367**, 671–676.
- 20 S. Horiuchi, Y. Tokunaga, G. Giovannetti, S. Picozzi, H. Itoh, R. Shimano, R. Kumai and Y. Tokura, *Nature*, 2010, **463**, 789–792.
- 21 H. Srinivasa Varaprasad, P. V. Sridevi and M. Satya Anuradha, *Adv. Powder Technol.*, 2021, **32**, 1472–1480.
- 22 W. H. Jung, H. Nakatsugawa and E. Iguchi, *J. Solid State Chem.*, 1997, **472**, 466–472.
- 23 H. P. Lv, Y. R. Li, X. J. Song, N. Zhang, R. G. Xiong and H. Y. Zhang, *J. Am. Chem. Soc.*, 2023, **145**, 3187–3195.
- 24 Y. M. You, W. Q. Liao, D. Zhao, H. Y. Ye, Y. Zhang, Q. Zhou, X. Niu, J. Wang, P. F. Li, D. W. Fu, Z. Wang, S. Gao, K. Yang, J. M. Liu, J. Li, Y. Yan and R. G. Xiong, *Science*, 2017, **357**, 306–309.
- 25 A. Jalalian, A. M. Grishin, X. L. Wang, Z. X. Cheng and S. X. Dou, *Appl. Phys. Lett.*, 2014, **104**, 0–5.
- 26 Y. Yang, W. Guo, K. C. Pradel, G. Zhu, Y. Zhou, Y. Zhang, Y. Hu, L. Lin and Z. L. Wang, *Nano Lett.*, 2012, **12**, 2833–2838.
- 27 C. R. Bowen, J. Taylor, E. Leboulbar, D. Zabek, A. Chauhan and R. Vaish, *Energy Environ. Sci.*, 2014, **7**, 3836–3856.
- 28 D. Berlincourt, H. Jaffe and L. R. Shiozawa, *Phys. Rev.*, 1963, **129**, 1009–1017.
- 29 M. H. Litt, C. H. Hsu and P. Basu, *J. Appl. Phys.*, 1977, **48**, 2208–2212.
- 30 X. Qiu, Y. Bian, J. Liu, Y. Xiang, T. Ding, W. Zhu and F. Z. Xuan, *IET Nanodielectrics*, 2022, **5**, 113–124.
- 31 S. K. Ghosh, T. K. Sinha, M. Xie, C. R. Bowen, S. Garain, B. Mahanty, K. Roy, K. Henkel, D. Schmeißer, J. K. Kim and D. Mandal, *ACS Appl. Electron. Mater.*, 2021, **3**, 248–259.
- 32 T. Furukawa, *Adv. Colloid Interface Sci.*, 1997, **71–72**, 183–208.
- 33 J. E. Wong, D. W. Bruce and T. H. Richardson, *Synth. Met.*, 2005, **148**, 11–14.
- 34 S. Q. Wu, M. Liu, K. Gao, S. Kanegawa, Y. Horie, G. Aoyama, H. Okajima, A. Sakamoto, M. L. Baker, M. S. Huzan, P. Bencok, T. Abe, Y. Shiota, K. Yoshizawa, W. Xu, H. Z. Kou and O. Sato, *Nat. Commun.*, 2020, **11**, 5–10.
- 35 P. Sadhukhan, S. Q. Wu, J. I. Long, T. Nakanishi, S. Kanegawa, K. Gao, K. Yamamoto, H. Okajima, A. Sakamoto, M. L. Baker, T. Kroll, D. Sokaras, A. Okazawa, N. Kojima, Y. Shiota, K. Yoshizawa and O. Sato, *Nat. Commun.*, 2021, **12**, 3–8.
- 36 N. Deepak, Z. Mallick, U. Sarkar, D. Mandal and R. K. Roy, *Chem. Mater.*, 2023, **35**, 3316–3328.